Optimization of $ZnGa_2O_4:Cr^{3+}$ Nanoparticles Synthesis Exhibiting Persistent Luminescence for Nanoplastic Labelling and Imaging in *Daphnia magna*

Adrian Drozdowski[1], Joanna Musiał[1], Anna Ekner-Grzyb[2], Kevin Soler Carracedo[1], Tomasz Grzyb[1]*

[1]*Department of Rare Earths, Faculty of Chemistry, Adam Mickiewicz University, Poznań, Uniwersytetu Poznańskiego 8, 61-614 Poznań, Poland*

[2]*Department of Cell Biology, Institute of Experimental Biology, Faculty of Biology, Adam Mickiewicz University, Poznań, Uniwersytetu Poznańskiego 6, 61-614 Poznań, Poland*

*E-mail: tgrzyb@amu.edu.pl

Abstract

Nano- and microplastic pollution is one of modern science's most pressing environmental challenges. Its presence has been reported in soil, water, air, aquatic species, and humans. Despite its widespread occurrence, tracking plastic particles within organisms remains challenging. Therefore, developing new visualization methods is crucial for understanding how nano- and microplastics are distributed and absorbed in biological systems. A promising solution lies in nanoparticles (NPs) capable of persistent luminescence, such as $ZnGa_2O_4:Cr^{3+}$, which, as labels, enable background-free detection in the first biological window range. In this work, we compare three different synthesis methods of the $ZnGa_2O_4:Cr^{3+}$ NPs, *i.e.,* precipitation, hydrothermal, and solvothermal, and their optimization for the best spectroscopic properties. The optimized NPs were then applied for polystyrene microparticles labeling and successfully used to track microplastic uptake and distribution in *Daphnia magna* as a model aquatic organism.

Keywords

Microplastics, nanoplastics, persistent luminescence, nanoparticles, bioimaging, *Daphnia magna*

1. Introduction

In recent years, nano- and microplastic pollution has emerged as one of the most urgent environmental problems. Numerous studies have demonstrated the presence of microplastics in soil, sea and freshwater, air, and a wide range of living organisms, including humans.[1–4] Moreover, microplastics can interact with other pollutants, such as antibiotics.[5,6] The adverse effects of

microplastics in aquatic systems lead to a decrease in microorganism populations, which can result in significant ecological imbalances.[7–10]

Consequently, there is a growing need to track the distribution of microplastics in living organisms to understand the mechanisms by which they interact with biological systems.[11–13] One promising approach involves marking microplastics with fluorescent materials, such as organic dyes or metal nanoparticles.[14–17] However, conventional fluorescent materials used in bioimaging have two significant limitations. First, the observed emission of the marking agent typically falls within the visible light range, where biological tissues significantly absorb the emitted light, reducing the signal intensity and hindering imaging. Second, the background autofluorescence in biological systems increases the detection limit due to signal noise.[18,19]

Persistent luminescence (PersL) nanoparticles (NPs) allow for the overcoming of the abovementioned drawbacks. PersL NPs have become popular in bioimaging in recent years thanks to the luminescence that persists after ceasing the excitation light source, which increases the signal-to-noise ratio and emission in the biological window range.[20] This property, in turn, allows for deeper tissue imaging.[21] One of the most studied PersL NPs for bioimaging are zinc gallate doped with chromium (III) ions ($ZnGa_2O_4:Cr^{3+}$, ZGO) particles.[21–24] Its popularity stems from the bright emission of Cr^{3+} ions at 700 nm (at the beginning of the first biological window), which lasts from minutes to hours, depending on the material's characteristics.[25,26] ZGO exhibits persistent luminescence (PersL) due to three key factors. First, its semiconductor nature, with a bandgap ranging from 4.4 to 5.0 eV, facilitates efficient energy migration within the material. Second, its crystal structure naturally accommodates defects that serve as energy traps, essential for the PersL phenomenon. Third, the presence of doping ions, specifically Cr^{3+}, enables bright emission and enhances the material's absorption in the UV-Vis range.[27] PersL in ZGO-based phosphors can be activated by a broad range of light sources, primarily UV and blue light, as well as white LEDs, allowing for the selection of an appropriate excitation source for specific applications.[28] Additionally, a significant advantage of ZGO as a bioimaging material is its ability to exhibit PersL after X-ray excitation, owing to its high transmissivity in biological tissues.[21,22,29]

Several ZGO synthesis methods have been reported to this day, with the first being solid state, which results in bulk material phosphor.[30] An advantage of this method is the relatively high yield of materials exhibiting long-lasting and bright luminescence. Unfortunately, micrometer-sized materials are typically less suitable for biological applications; therefore, it is essential to produce

nanomaterials for bioimaging. Currently, three main synthesis approaches exist for preparing uniform ZGO nanoparticles: the precipitation (sol-gel),[26,31] hydrothermal,[21,32,33] and the solvothermal method.[22] Each of the above synthesis pathways has its advantages, but the products differ in terms of PersL decay time or particle morphology. Several works have compared ZGO to other PersL phosphors, but there has been no comparison between different synthesis methods of ZGO NPs up to this day. Moreover, previously reported works focused only on showing bioimaging using ZGO-based materials in tissues, while the possibility of their application in microplastic labeling to visualize its potential uptake in living organisms has been overlooked.[25,34–36]

Using ZGO NPs as PersL markers of microplastic particles can contribute to a deeper understanding of the impact of microplastic pollution on natural ecosystems and human health. Microplastics have already been reported to cause adverse effects in living organisms,[37] and the finest particles – small microplastics (<100 μm) and nanoplastics (<1 μm) – are hypothesized to be an even greater threat due to their ability to transfer across biological membranes.[38] However, their small size and chemical composition make microplastics challenging to detect and monitor in environmental and biological samples.[39–41] Hence, in this study, ZGO NPs are used as a PersL marker to investigate the uptake of plastic particles in a small planktonic crustacean, *Daphnia magna*. These low-level trophic chain organisms serve as suitable biomaterials for studying the ecological risks and toxicity of microplastic. Therefore, they are used as standard experimental genus. What is more, there is a great need to study the mechanism of influence of microplastic pollution in freshwater on *D. magna* as it can affect their population level, behavior, feeding, development, and reproductive ability.[42,43]

This work compares three synthesis methods of $ZnGa_2O_4:Cr^{3+}$ NPs (precipitation, hydrothermal, and solvothermal) regarding PersL time decay and luminescence intensity. Additionally, we optimize the Zn:Ga ratio and Cr^{3+} doping levels to enhance PersL decay time. Next, a novel application of PersL NPs in microplastic labeling for bioimaging was performed. Finally, we demonstrate the tracking of ZGO NP-labelled microplastics in *D. magna* as a model aquatic organism as a first-ever example of bioimaging of microplastic in aquatic organisms using PersL NPs.

2. Experimental section

2.1. Materials and methods

For $ZnGa_2O_4$ NPs synthesis, the following reagents were used: $Zn(OAc)_2$ (99.99%), $Zn(NO_3)_2 \cdot 6H_2O$ (>99%) (Sigma Aldrich, Poland), $Cr(NO_3)_3 \cdot 9H_2O$ (99.99%, Acros Organics, Poland) $Ga(NO_3)_3 \cdot xH_2O$ (99.99%, Merck, Poland), LiOH (>98%, Honeywell, Poland), NaOH (98.8%, Avantor, Poland), $NH_{3(aq)}$ (25% water solution, Stanlab, Poland), n-hexane (99%, Avantor, Poland), oleic acid (90%, Alfa Aesar, Poland). For plastic microparticles synthesis, toluene (99.5%, Avantor, Poland) and expanded polystyrene from a packaging material were used.

For the autoclave synthesis, DAB-2 from Berghof Products + Instruments GmbH was used. Microplastic materials were prepared using the CryoMill (Retsch GmbH), a ball mill connected to a liquid nitrogen cooling system.

Structural and morphological analysis of the materials was performed using Bruker AXS D8 Advanced diffractometer with Cu Kα1 (λ = 0,154 nm) in a range of 2θ 10° - 80°. Colloidal sizes of the obtained materials were determined using dynamic light scattering (DLS) using a Malvern Zetasizer Nano ZS equipped with a laser of 632.8 nm wavelength in backward scattering mode (173°) at 25°C. The materials' dispersions were diluted with deionized water to reach the operating concentration range. The measurements were performed in triplicate, each with 12 runs of 10 s in polystyrene cuvettes.

The geometric size (Feret diameter) and morphology of the materials and their uptake in *Daphnia magna* were determined using a Nikon Eclipse Ti2-U inverted fluorescent microscope. The materials were visualized using the Nikon CFI Plan Apochromat Lambda D 20× (N.A. 0.8, W.D 0.8 mm) and Nikon CFI Plan Apochromat Lambda D 60× Oil (N.A. 1.42, W.D. 0.15 mm) objectives. The samples were prepared by dropping 50 µL of the DLS dispersion on a microscope slide. For Feret diameter calculation, pictures were taken using the 20× objective in brightfield mode in 5 sample areas. ImageJ software (version 1.54g) was used to process the image and perform calculations. The uptake and distribution of the particles in D. magna were visualized using Nikon CFI Plan Achromat 4× (N.A. 0.10, W.D. 30.0 mm) and Nikon CFI Achromat 10× (N.A. 0.25, W.D. 6.2 mm) objectives, in brightfield and fluorescence modes (DAPI and with longpass 600 nm filter).

Transmission electron microscopy (TEM) imaging Hitachi HT7700 microscope operating at 100 kV was used to confirm the morphology of ZGO NPs and their incorporation into the polymer matrix.

For spectroscopic analysis of samples, a PIXIS:256 Digital CCD Camera with an SP-2156 Imaging Spectrograph (Princeton Instruments) and QuantaMaster™ 40 spectrophotometer (Photon Technology International) equipped with an R928 photomultiplier tube (Hamamatsu) were used. As an excitation source (375 nm), a 2.8 W CW diode laser (CNI) and light-emitting diode centered at 375 nm were used. The obtained material's excitation and emission spectra measurements were measured using a Hitachi 7000 (Hitachi High Technologies America, Inc.) fluorescence spectrometer equipped with a monochromated Xe-arc lamp as the excitation source.

2.2. Synthesis of $ZnGa_2O_4:Cr^{3+}$ NPs via precipitation method

$ZnGa_2O_4$ NPs were obtained via the precipitation method (sol-gel process) described in previous reports, with necessary modifications.[26] First, 50 mL of ethanol and 2.5 mmol of $Zn(OAc)_2$ were placed in a round-bottom flask connected to a reflux condenser. The mixture was stirred for one hour at

78 °C until all the powder was dissolved. Then 60 mL of distilled water with previously dissolved 5.5 mmol of $Ga(NO_3)_3 \cdot xH_2O$ and 0.01 mmol of $Cr(NO_3)_3 \cdot 9H_2O$ were added, and the mixture was stirred for 30 min at room temperature. Next, 15 mL of water with 12.5 mmol of LiOH was added dropwise with a 1 mL/min flux. The resulting cloudy mixture was stirred at room temperature for 24 h. Next, the NPs were collected with centrifugation (8000 g, 10 min) and washed with distilled water three times. The final product ($ZnGa_2O_4$:0.4%Cr^{3+}) was obtained after drying the material at 80 °C for 72 h.

2.3. $ZnGa_2O_4$ NPs synthesized via hydrothermal method

According to previous reports, ZGO NPs were synthesized via a hydrothermal method with a few modifications.[21] First, 1.5 mmol $Zn(NO_3)_2 \cdot 6H_2O$, 3.3 mmol $Ga(NO_3)_3 \cdot xH_2O$, and 0.006 mmol $Cr(NO_3)_3 \cdot 9H_2O$ were dissolved in 20 mL of distilled water. Next, the pH of the mixture was set to 7.7 using $NH_{3(aq)}$. The pH stabilized at 7.5 after 30 min, and the obtained solution was transferred to a Teflon-lined autoclave dish and kept at 120 °C for 24 h. The resulting mixture was centrifuged (8000 *g*, 10 min), the precipitate was redispersed in 10 mL of water and 25 mL of ethanol and centrifuged again (8000 g, 10 min). The final product, $ZnGa_2O_4$:0.4%Cr^{3+}, was dried at 80 °C for 72 h.

2.4. $ZnGa_2O_4$ NPs synthesized via solvothermal method

The solvothermal method was applied to obtain ZGO NPs as a modification of the previously reported liquid-solid-solution method.[22] First, 1 mmol $Zn(NO_3)_2 \cdot 6H_2O$, 2.2 mmol $Ga(NO_3)_3 \cdot xH_2O$ and 0.004 mmol $Cr(NO_3)_3 \cdot 9H_2O$ were dissolved in 3 mL of distilled water. In another flask, 15 mmol of NaOH was dissolved in 8 mL of water and 18 mL of ethanol. Next, the metal salts solution was added dropwise to the intensively stirred solution of NaOH. After 30 min of stirring, 6 mL of oleic acid was added dropwise, and the mixture was stirred again for 30 min. Next, the mixture was transferred to a Teflon-lined autoclave dish and kept at 210 °C for 16 h. The resulting dark yellow mixture was centrifuged (8000 g, 5 min), the precipitate was dispersed in 10 mL of n-hexane and 25 mL of ethanol, and centrifuged again (8000 g, 5 min). The obtained material was redispersed in 15 mL of n-hexane and centrifuged at low revolution speed (3000 g, 5 min) to separate the smallest nanoparticles. The supernatant was mixed with 25 mL of ethanol and centrifuged (8000 g, 10 min). The final product was dried at 80 °C for 72 h, dispersed in a mixture of n-hexane and oleic acid (v/v = 20:1), and taken for further analysis. In this work, ZGO NPs with different Cr^{3+} doping concentrations and Zn^{2+} to Ga^{3+} ratios were obtained by changing the metal salts ratio and keeping all the other synthesis parameters constant.

Before the biological uptake tests of the ZGO NPs with 0.4%$_{mol}$ of Cr^{3+} ions and Zn^{2+}:Ga^{3+} (ratio 1:2) in *Daphnia magna*, the surface of the obtained ZGO NPs was modified to allow their dispersion in water. The ZGO NPs were treated with diluted HCl solution to remove oleic acid from their surface and then redispersed in deionized water. As a result, water colloids of 20 mg/mL were obtained.

2.5. Preparation of polystyrene particles labeled with $ZnGa_2O_4$:Cr^{3+}

First, 735 mg of polystyrene (PS) was dissolved in 5 mL of toluene at 60 °C. Then, 15 mg of dried ZGO NPs (with 0.4%$_{mol}$ of Cr^{3+} ions and Zn^{2+}:Ga^{3+} ratio 1:2) were added, and the solution was stirred for 60 min at 60 °C. After that, the mixture was sonicated for 15 min and stirred again for 60 min at 60 °C. Next, the toluene was evaporated on a heating plate, and the resulting solid, the bulk plastic doped with ZGO NPs, was crushed into small pieces and placed in the CryoMill. The material was milled with 20 ZrO_2 balls (5 mm diameter) in 6 milling cycles consisting of 5-min milling at 30 Hz and 1-min cooling at 5 Hz). The obtained fine powder, PS:2% ZGO, was suspended in demineralized water 2.5 mg/mL) and tested in *D. magna*.

2.6. Bioimaging of *Daphnia magna*

For bioimaging, *D. magna* was incubated in the presence of ZGO NPs and PS:2% ZGO. Stock solutions of both particles at a concentration of 2.5 mg/mL, were prepared by adding 25 mg of the materials to the 10 mL of water and dispersed *via* sonication in an ultrasound bath for 30 s. Next, the solutions were diluted to 1 mg/mL, using a medium with green microalgae *Raphidocelis subcapitata*. Individuals treated with a medium without NPs were used as a control. After 72 h of incubation at a laboratory-controlled condition (20 ± 2 °C; photoperiod 16:8 h light: dark), all of the daphnias were washed by immersion in distilled water and then frozen. Immediately before the visualization, *D. magna* were thawed and observed under the fluorescence microscope (Nikon ECLIPSE Ti2).

3. Results and Discussion

This section presents our investigation of ZGO PersL materials aimed at determining the optimal synthesis method and ion ratios in relation to PersL properties. Identifying the best material was crucial for efficient microplastic labeling and successful bioimaging. Fig. 1 illustrates a schematic representation of the investigation procedures. First, three synthesis methods were selected based on previous reports demonstrating the feasibility of synthesizing small and monodisperse PersL NPs. Using these methods, three analogous materials were obtained with identical ion ratios, chosen based on current knowledge. Subsequently, structural, morphological, and spectroscopic analyses were conducted to determine the most promising synthesis method, which was identified as the solvothermal method. Based on this finding, two successive series of ZGO were synthesized with varying ion concentrations. The resulting products were characterized, leading to the identification of the optimal material for microplastic labeling. Next, a top-down preparation method was chosen as the best approach for emulating the actual environmental process of microplastic formation. This method was used to obtain labeled polystyrene micro- and nanoparticles. In the final step, Daphnias were cultivated in an environment containing labeled microplastics and subsequently used for bioimaging to visualize microplastic uptake and distribution within this model organism.

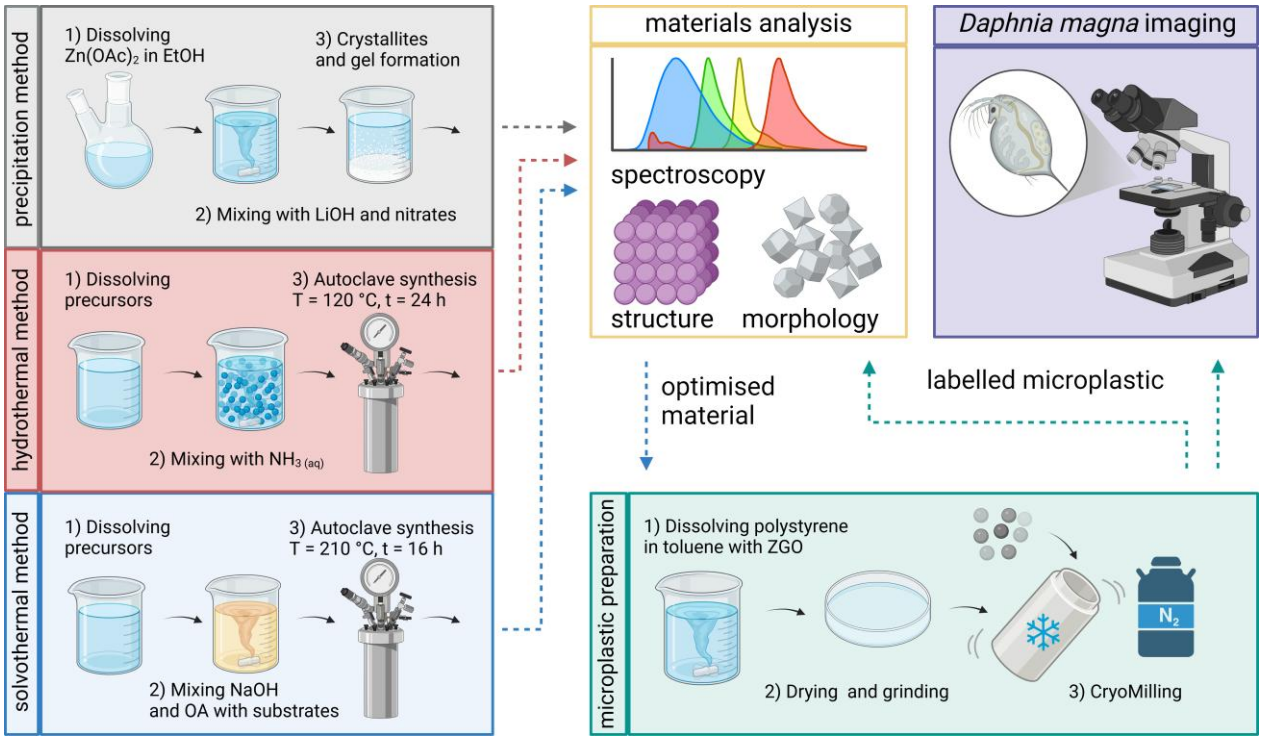

Fig. 1. Schematic representation of the investigation procedures undertaken.

3.1. Structure and morphology of the synthesized NPs

Synthesized $ZnGa_2O_4$:0.4%Cr^{3+} NPs (hereafter referred to as ZGO unless stated otherwise) were first characterized with X-ray powder diffraction (XRD) to confirm the structure and purity of obtained materials. Pure-phase $ZnGa_2O_4$ NPs were successfully obtained through all three synthesis methods, as evidenced by the diffraction patterns matching well with the reference pattern (Fig. 2 (a)). In each material, characteristic broadening of peaks was observed, which, according to the Scherrer formula, is caused by the small grain size of obtained nanocrystals. Nevertheless, the peaks were the sharpest and best separated in the case of the nanoparticles obtained *via* the solvothermal method, which suggests the best crystallinity among the three studied synthesis routes. Fig. 2 (b) shows the crystal structure of the studied materials. $ZnGa_2O_4$ crystallizes in a normal spinel oxide structure (AB_2O_4) with a space group of $Fd\bar{3}m$. In this cubic close-packed oxygen anions structure, ½ of the octahedral sites are occupied by B^{3+} ions, and one-eight of the tetrahedral sites are occupied by A^{2+} ions. Although, the spinel shows a tendency for slight inversion of site occupation as approximately 3% of Zn^{2+} and Ga^{3+} ions occupy B^{3+} and A^{2+} sites, respectively. Cr^{3+} ions substitute only Ga^{3+} in the crystal structure as the ions share similar ionic radii (61.5 and 62 pm, respectively) and charge.

Furthermore, Cr^{3+} ions are stabilized in octahedral coordination, which energetically favors substitution at Ga^{3+} sites rather than Zn^{2+}.[30,44]

Transmission electron microscopy (TEM) imaging was performed to analyze the structure of the synthesized materials further. Uniform and monodisperse NPs were obtained for each synthesis method, as shown in Figs. 2 (c-e). Notably, the smallest and best-dispersed NPs were achieved using the solvothermal method, with an average size of 2.8 ± 0.6 nm. In contrast, the precipitation and hydrothermal methods produced larger and more agglomerated crystals, measuring 4.7 ± 1.4 nm and 5.7 ± 1.2 nm, respectively. Despite slight differences in the sizes of NPs, the overall structures and morphologies of the products are very similar, enabling meaningful comparisons of their luminescence and other properties. The absence of high-temperature treatment during synthesis contributed to the exceptionally small crystal sizes (<10 nm) observed in all samples. Despite that, obtained NPs' surfaces were not functionalized and therefore formed significantly bigger agglomerates in water colloids (Fig. S2). Nevertheless, this behavior of NPs does not affect their further application in microplastic labeling.

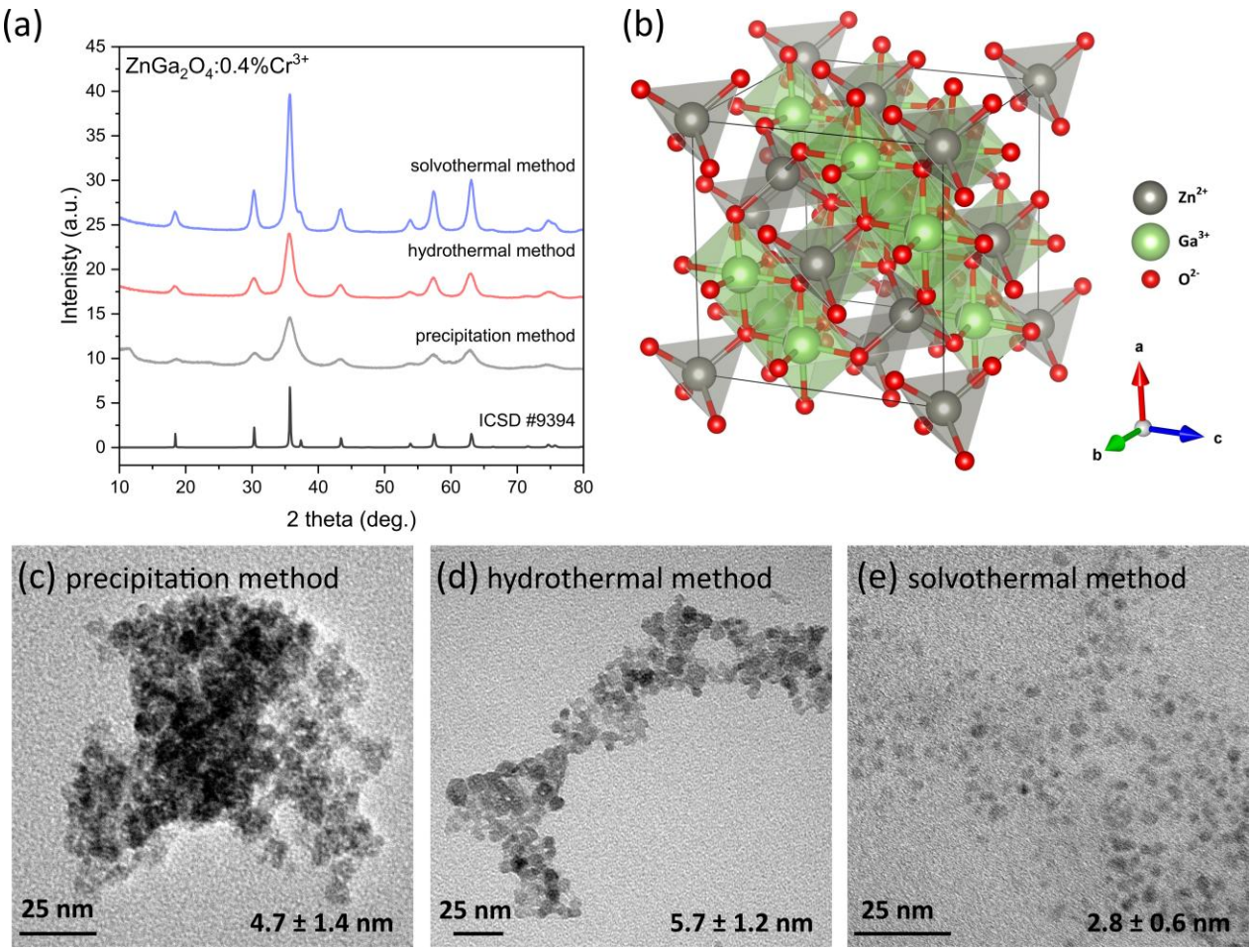

Fig. 2. (a) XRD patterns of the $ZnGa_2O_4$:0.4%Cr^{3+} NPs synthesized using precipitation, hydrothermal, and solvothermal methods, compared with the reference pattern from the ICSD crystallography database; (b) crystal structure of the $ZnGa_2O_4$; (c-e) TEM images of the products obtained by the three synthesis methods, including the average sizes of the NPs calculated from the images (see Fig. S1 for histograms of the NP size distributions).

The solvothermal method was also employed to optimize the Zn:Ga ratio and the concentration of the Cr^{3+} dopant, as various sources suggest differing molar percentages of chromium ions as optimal. The crystal structure remained unchanged for all synthesized materials, with no additional impurities detected (Fig. 3 (a)). Increasing the Cr^{3+} concentration did not result in any observable changes in crystallinity or unit cell dimensions. When the Zn:Ga ratio was modified (Fig. 3 (b)), a slight shift in the maximum of the most intense reflection ($2\theta = 36°$) was observed. This shift may be attributed to minor variations in unit cell parameters caused by the slight difference in ionic radii between Zn^{2+} and Ga^{3+} ions. However, these changes in the Zn:Ga ratio did not significantly

affect the nanoparticle sizes or morphology. As a result, the luminescent properties of the materials can be compared independently of structural changes, allowing for the investigation of the effects of varying ionic ratios on luminescence. As the ICP-MS analysis shows (Table S1), changes in actual material composition follow the change in ion ratios used in the synthesis for these two series of materials. For all of the materials in these two series, about 90-95% of the Ga^{3+} ions used are incorporated into the structure compared to Zn^{2+} ions. Additionally, on average, 70% of the Cr^{3+} ions used in the synthesis are built into the material. Despite being crucial for further planning ZGO-based materials synthesis, the above information does not affect analyzed trends and the determination of the most suitable material for microplastic labeling.

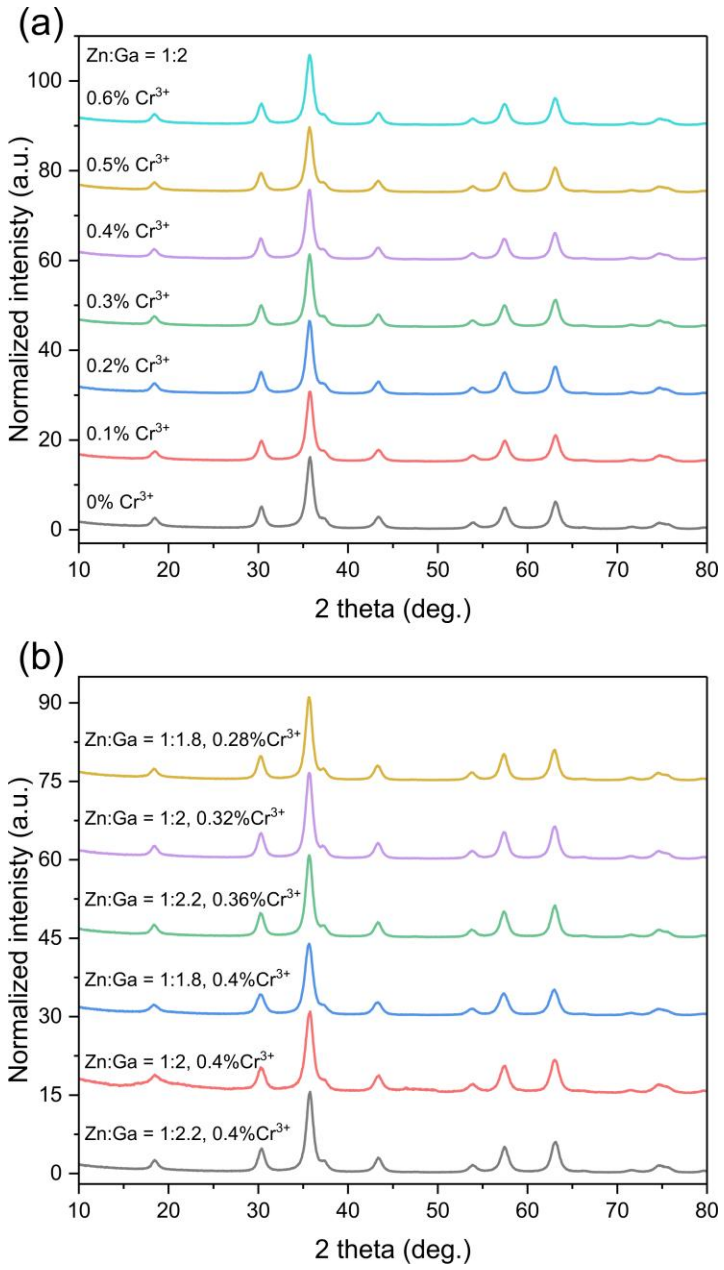

Fig. 3. Comparison of the XRD patterns of the $ZnGa_2O_4$ NPs synthesized using the solvothermal method: (a) shows the patterns for products with different concentrations of Cr^{3+} ions, and (b) presents the patterns for products obtained using varying Zn^{2+} : Ga^{3+} : Cr^{3+} ratios in the reaction mixture.

3.2. Spectroscopic properties of $ZnGa_2O_4:Cr^{3+}$ NPs

The luminescent properties of ZGO materials synthesized via different methods were analyzed by examining their excitation spectra at an emission wavelength of λ_{em} = 695 nm. All samples exhibited

the same excitation bands (Fig. 4 (a)). The first broad band ranges from 200 to 360 nm. Previous reports show that this band is generated through three different transitions.[26,44] First is the absorption band of the matrix related to the charge transfer from the valence band (VB) to the conduction band (CB), with the maximum at 275 nm (4.5 eV). Other works have shown that depending on the synthesis method, the energy of the VB → CB transition can vary from 4.4 to 5.0 eV. Two remaining bands with maxima at 250 and 325 nm come from Cr^{3+} ions transfers from the ground state of [4A2 (4F)] to [4T1 (4P)] excited state and CB of the matrix, respectively. The blue band in absorption spectra with a maximum at 420 nm also results from [$^4A_2$ (^4F)] to [$^4T_1$ (^4F)] Cr^{3+} transition.

Fig. 4 (b) presents emission spectra of obtained ZGO materials excited at 275 nm. In all cases, two main emission bands are observed. The broad band ranging from 400 to 600 nm is attributed to the electrons (e^-) in CB recombining with different types of holes (h^+) at defects or traps in the lattice.[44] The main emission band with a maximum at 695 nm comes from the Cr^{3+} transition from the first excited state [^2E (^2G)] to the ground state of [$^4A_2$ (^4F)]. The band has two main peaks with maxima at 695 and 715 nm.[26] The first one can be attributed to the Cr^{3+} transition in unperturbed octahedral sights (688 nm) and with one defect in the first cationic neighbor (695 nm). The second maximum arises from the Stokes band (708 nm) overlapping with the phonon sideband at 715 nm. The bands are not well-resolved due to the relatively low crystallinity and small crystal sizes of the not-annealed ZGO NPs.[26] Among the samples, the ZGO material prepared via the solvothermal method exhibited the brightest Cr^{3+} luminescence despite consisting of the smallest NPs. This highlights the effectiveness of the solvothermal method in enhancing luminescent properties, even with reduced crystal size.

The emission spectra of ZGO samples with varying Cr^{3+} concentrations (Fig. 4 (c)) reveal that the brightest luminescence is achieved at Cr^{3+} doping levels of $0.3\%_{mol}$ and $0.4\%_{mol}$. In the undoped ZGO matrix, only the band attributed to electron-hole recombination is observed, with no Cr^{3+} emission present. As the Cr^{3+} concentration increases, the emission intensity rises, reaching a maximum at 0.3%mol, after which it begins to decrease. This decrease at higher doping levels is attributed to concentration quenching, where excessive Cr^{3+} ions lead to non-radiative energy transfer between neighboring dopant ions. Fig. 4 (d) shows the emission spectra of ZGO samples with different Zn:Ga ratios. The brightest luminescence was observed in samples with the stoichiometric ratio of Zn:Ga (1:2) in both series—those with a fixed Cr^{3+} concentration and those with decreasing

Cr^{3+} content. Additionally, samples doped with 0.4%$_{mol}$ Cr^{3+} consistently exhibited brighter luminescence than those with proportionally reduced doping.

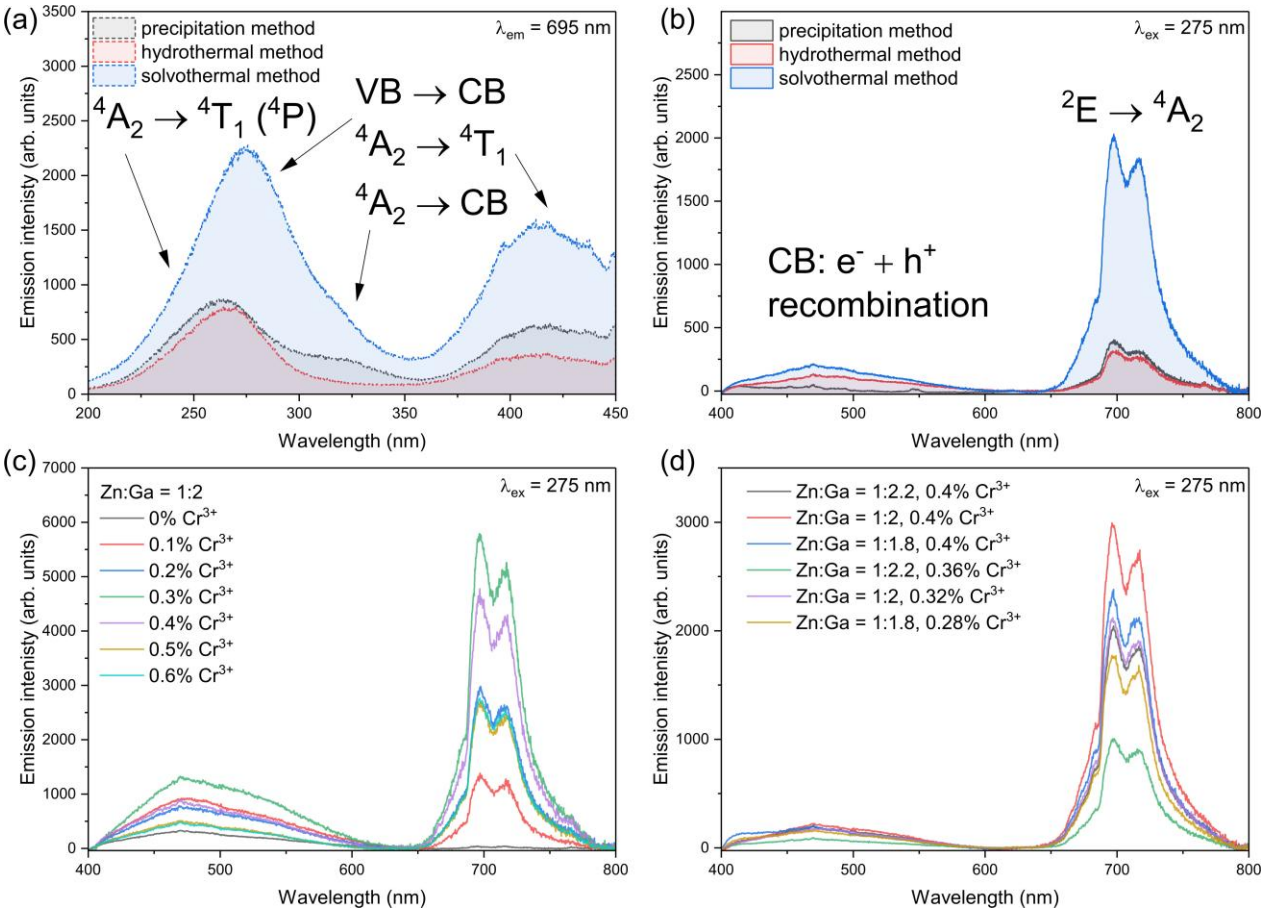

Fig. 4. Spectroscopic properties of $ZnGa_2O_4$:Cr^{3+} NPs; (a) and (b) show the excitation and emission spectra of NPs synthesized by three different methods; (c) and (d) presents emission spectra of NPs prepared by the solvothermal method by using various concentrations of Cr^{3+} ions (c) or ratio between reagents (d).

Beyond emission spectra and brightness, the most critical property characterizing NPs showing persistent luminescence is their decay time of PersL. Lifetimes of the luminescence were determined by fitting the decay curves to a bi-exponential equation with $R^2 > 0.98$. The decay intensity is well-described by the equation: $I = A_1 e^{-\frac{t}{\tau_1}} + A_2 e^{-\frac{-t}{\tau_2}}$ where I is emission intensity, A_1 and A_2 are experimental constants, t is time, and τ_1 and τ_2 are lifetimes associated with two different types of traps.[30,45] The presence of two components in the decay curves arises from the mechanism of PersL in the ZGO matrix. As reported previously, the matrix has two types of electron traps, located

approximately 0.97 eV and 0.75 eV below the conduction band (CB). The traps closer to the CB are characterized by τ_1, are emptied more rapidly due to the lower energy required for electron release. Conversely, deeper traps, described by τ_2, exhibit far longer luminescence decay times.[26] Fig. 5 (a) compares the persistent luminescence decay in ZGO samples synthesized via three different methods. The longest-lasting luminescence was observed in the material synthesized using the solvothermal method, with lifetimes of τ_1=0.5 s and τ_2=7.4 s. The materials synthesized via precipitation and hydrothermal methods exhibited shorter lifetimes. The precipitation method resulted in a product with τ_1=0.3 s, τ_2=2.2 s, whereas hydrothermal method in material with τ_1=0.5 s, τ_2=10.2 s. These differences suggest that the solvothermal method produces deeper and more effective traps, enhancing the duration of persistent luminescence.

Comparing the PersL decay of ZGO samples synthesized via the solvothermal method with varying Cr^{3+} doping levels (Fig. 5 (b)) shows that the luminescence decay remains relatively consistent across doped samples. However, the longest lifetimes are observed in the sample doped with 0.4%$_{mol}$ Cr^{3+}. Beyond this concentration, the luminescence lifetimes begin to decrease, likely due to concentration quenching. In the undoped ZGO matrix, the PersL is significantly weaker and primarily attributed to the broad emission arising from electron-hole recombination in the host lattice (as described previously). For materials with varying Zn:Ga ratios, longer-lasting luminescence is observed in samples with a reduced Ga^{3+} concentration (Fig. 5 (c)), but only when the Cr^{3+} concentration is proportionally reduced. In contrast, when Cr^{3+} concentration is held constant, luminescence intensity decreases as Ga^{3+} content decreases. This phenomenon may be explained as follows: Non-stoichiometric compositions with reduced Ga^{3+} introduce additional lattice defects, creating more electron traps at varying depths. These traps can enhance energy storage within the material, leading to longer-lasting luminescence. Similar effects have been reported in other persistent luminescence phosphors, where lattice defects act as trap sites for electron storage.[46] However, reducing Ga^{3+} while maintaining a fixed Cr^{3+} concentration increases the relative amount of Cr^{3+} in the material, which can promote non-radiative energy transfer between dopant ions, leading to quenching of luminescence. Based on these results, the optimal ion concentrations for achieving the brightest and longest-lasting luminescence in NPs synthesized via the solvothermal method (without annealing) are Zn:Ga:Cr = 1:1.8:0.0028.

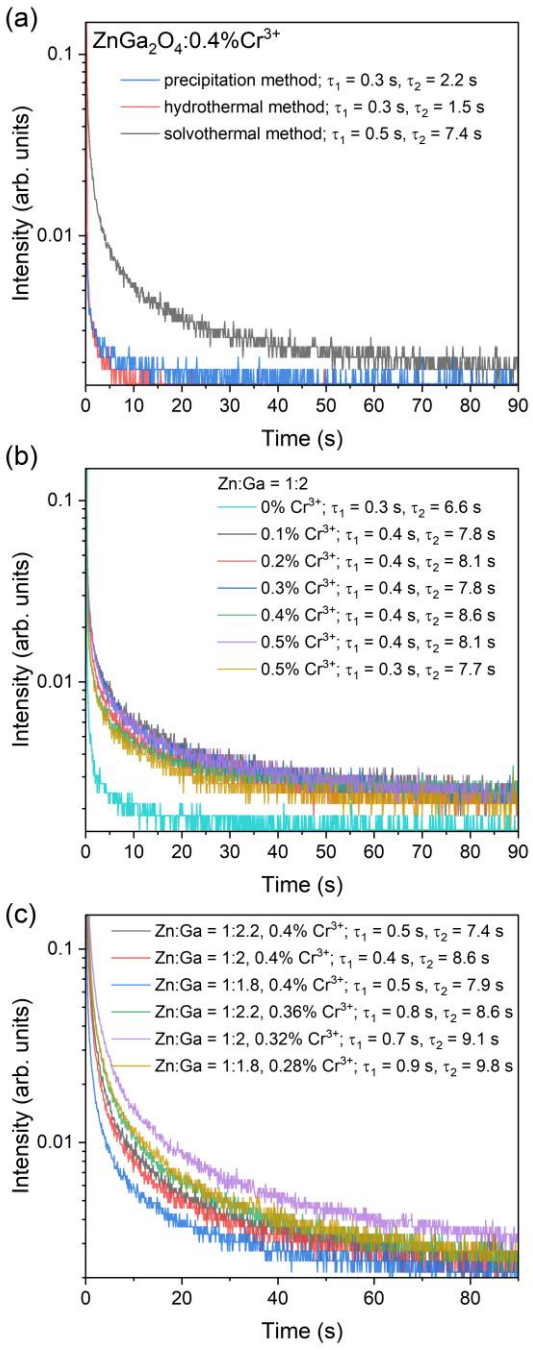

Fig. 5. Afterglow decay measurements under 375 nm laser excitation (with an irradiation time of 10 seconds): (a) dependence of decay times on the synthesis method of $ZnGa_2O_4$:0.4%Cr^{3+}; (b) decays measured for samples prepared using the solvothermal method with varying concentrations of Cr^{3+} ions; (c) afterglow decays of $ZnGa_2O_4$:0.4%Cr^{3+} nanoparticles synthesized by solvothermal method with different substrate concentrations.

3.3. Application of $ZnGa_2O_4:Cr^{3+}$ NPs in nanoplastic labeling and bioimaging

The ZGO NPs obtained through optimization were used to label polystyrene microparticles to make them visible in *D. magna*. The selected ZGO NPs exhibited not only the best luminescent properties for this purpose but also appropriate nanometric sizes, enabling their uniform distribution within the polystyrene microparticles. Additionally, their hydrophobic surface (due to the presence of oleic acid molecules) facilitated incorporation into the polymer microparticles.

Physicochemical characterization of the PS: 2% ZGO particles, including their size, morphology, incorporation of the ZGO NPs into the polymer matrix, and luminescence properties, is reported in the Supporting Materials (Figs. S2-S7).

The TEM images confirmed the incorporation of the ZGO NPs into polystyrene (Fig. S3). Despite relatively low dopant content, 2% (w/w), the ZGO NPs are well distributed throughout the polymer matrix. Cryomilling of the bulk PS: 2% ZGO led to obtaining randomly shaped microparticles. Nevertheless, TEM images indicate that the cryomilling procedure, which, as described in the Methods section, consisted of six 1-min milling cycles at 30 Hz, allows obtaining particles that can be classified as 'small microplastics.' This result supports evidence from previous works on small microplastic and nanoplastic reference materials prepared via a top-down approach, summarized in a recent review article.[47]

The size of the particles was determined via DLS and optical microscopy. Fig. S4 presents the hydrodynamic size distribution of the PS: 2% ZGO microparticles measured using DLS, whereas Fig. S6 shows the geometric size distribution – Feret diameter – derived from processed brightfield microscope images (Fig. S5). The average particle sizes determined by DLS were 297, 555, and 456 nm, and the dispersity index values were 0.980, 0.713, and 0.873 in measurements 1, 2, and 3, respectively (Fig. S4). No particles larger than 1 µm were reported in the DLS analysis, which suggests that the water dispersion of PS: 2% ZGO could be considered nanoplastic in terms of plastic particle size classification.[48] The shift in the particle size range, from 250-400 nm in the first measurement (m1) to 350-600 nm in measurements 2 and 3, as well as the high dispersity index values, indicate strong agglomeration of the particles during the measurements. These values are consistent with other plastic particle size ranges reported in other works on top-down preparation of micro- and nanoplastic reference materials.[49–51] Although DLS is a valuable tool for quick determination of the size (or size range) of the finest plastic particles dispersed in water, these data must be interpreted with caution. DLS measures the hydrodynamic diameter (D_h) that represents the size of a solvated

particle, assumes a spherical shape of the particles, and that the sample forms a stable dispersion. These assumptions are not met in the case of polystyrene-based particles obtained via cryomilling since this top-down approach results in the formation of non-uniform samples of randomly shaped particles. Top-down prepared samples represent the actual, environmental plastic microparticles better than commercial latexes produced via a bottom-up synthesis because the cryomilling process resembles macroplastic weathering via mechanical abrasion.[1] In addition, the finest PS particles tend to agglomerate on the water surface over time and even attach to and creep up the walls of the DLS cuvette, which can affect the measurement.[49]

To provide the most accurate determination of the actual PS: 2% ZGO size distribution, we support the DLS analysis with particle size calculations based on the microscopy images obtained using the fluorescent microscope in the brightfield mode. Five images showing different areas of the sample were collected using the 20× Plan Apo objective and fixed image acquisition settings. The acquired images were processed using the same background threshold settings, resulting in the presentation of the particle outlines (Fig. S5) and the Feret diameter distribution (Fig. S6). Although rarely used in plastic particle size determination, the Feret diameter, defined as the longest distance between any two points along the selection boundary (also known as maximum calliper), can be a good measure to report the size of randomly shaped particles accurately. The average Feret diameter for all the particles recognized in all five images was 2.135 µm (Table S2), with the values varying from 1.618 µm for the particles in Fig. S5(a) to 2.696 µm in Fig. S5(b). The relative frequency of the particle count was plotted to compare the Feret distribution profiles between the images despite different particle counts. As shown in Fig. S6, the distribution plots overlap, indicating a similar Feret diameter distribution of the particles detected in each image. Moreover, the cumulative per cent analysis showed that particles smaller than 1 µm constitute 16 to 38% of the particles (corresponding to Fig. S5(c) and Fig. S5(a), respectively), representing a considerable fraction of the sample.

The luminescence properties of PS: 2% ZGO are presented in Fig. S7. The emission spectra of PS: 2% ZGO under UV excitation consist of two main bands (Fig. S7(a)). A broad band emerges from the polymer fluorescence and light scattering on microparticles in the visible light range. At 700 nm is the characteristic band attributed to the Cr^{3+} $^2E \rightarrow {}^4A_2$ transition in ZGO PersL NPs. Additionally, obtained labeled plastic material showed bright PersL despite the low doping percentage of used PersL NPs (Fig. S7(b)).

These emission properties are visualized in Fig. S7(c-e) as a set of fluorescence microscopy images of the PS: 2% ZGO sample acquired in brightfield and fluorescence mode using the 60× objective. The emission of the ZGO NPs (Fig. S7d) overlaps with the shape of the polystyrene microparticles (Fig. S7c) and is presented as an overlay image in Fig. S7e. This, in addition to TEM images, confirms the successful incorporation of the ZGO NPs into the polystyrene matrix.

Daphnias are excellent model organisms for imaging the uptake of nanoparticles due to their transparency. In our previous reports, we demonstrated that nanoparticles exhibiting the upconversion phenomenon are clearly visible in the intestines of Daphnia, allowing for the assessment of their uptake as well as the evaluation of temperature inside this organism.[52,53] Daphnia primarily ingest algae from their environment, which serves as their primary food source. At the same time, or rather incidentally, they also uptake various contaminants present in the water, including, as in our case, microplastic particles.

Figs. 6 (a) and (c) show microscope images of Daphnias under white light illumination (brightfield) in the presence of $ZnGa_2O_4:Cr^{3+}$ and polystyrene microparticles labeled with $ZnGa_2O_4:Cr^{3+}$ NPs, respectively. In the brightfield images, it is visible that the intestines of the organisms are filled. Figs. 6 (b) and (d) present the fluorescence of the organisms in the blue spectrum under 375 nm LED illumination. In both cases, the entire *D. magn*a exhibits autofluorescence, making it difficult to distinguish the locations where NPs or PS microparticles have accumulated. Only after using a 600 nm long-pass filter(Figs. 6 (e) and (g)) was it possible to observe the emission of Cr^{3+} ions (under continuous illumination with a 375 nm LED source), which, as previously shown in Fig. 4, falls within the 650–800 nm range. As can be seen in Figs. 6 (c) and 7 (c), most of the NPs and PS microparticles have accumulated in the intestines of the Daphnia.

After switching off the light source, the excited ZGO NPs exhibit short-lived afterglow luminescence, intense enough to be observed under the microscope. Figs. 6 (f) and (g) show weak emission above 600 nm—in both cases, where the images were recorded for 2 seconds after switching off the 375 nm LED source excitation. In Fig. 6 (f), it is clearly visible that using ZGO NPs alone enables a much more intense emission. In Fig. 6 (h), the emission of labeled polystyrene is significantly weaker due to the fact that it contains only 2 wt% of ZGO NPs. Nevertheless, the emission is still distinguishable from the background, confirming the presence of the investigated microplastic in the intestines of *D. magna*. Additionally, Daphnias incubated with PS: 2% ZGO were imaged using the 10× objective to visualize better their guts containing microplastics (see Fig. S8).

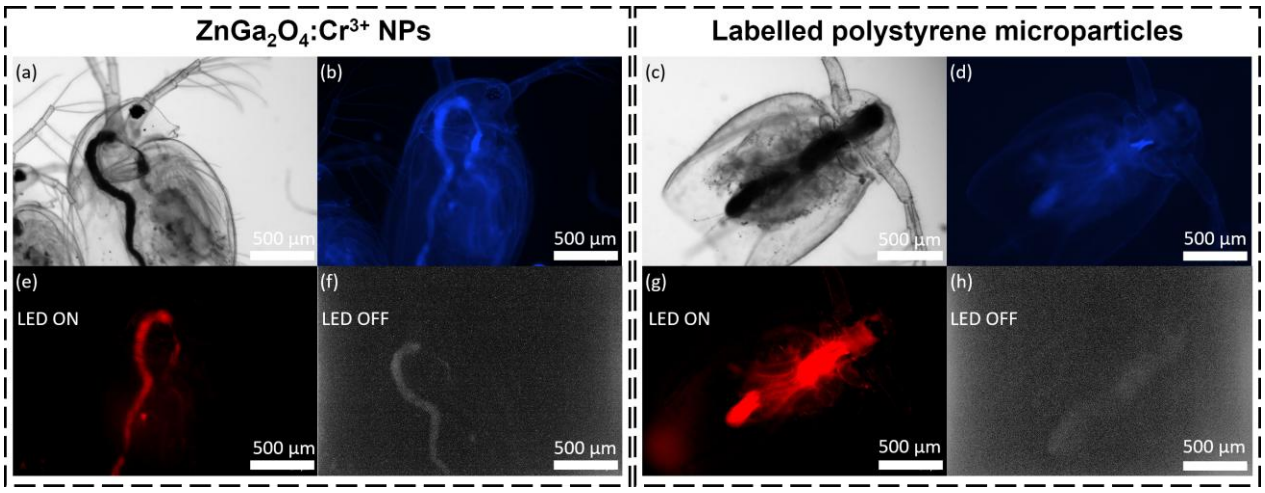

Fig. 6. (a, c) Microscope images of *Daphnia magna* incubated in the presence of $ZnGa_2O_4:Cr^{3+}$ NPs and of polystyrene microparticles labeled with $ZnGa_2O_4:Cr^{3+}$ NPs (both at a concentration of 1 mg/mL) in brightfield mode, respectively. (b, d) Autofluorescence mode under 375 LED excitation. (e, g) Emission of Cr^{3+} ions visualized using a 600 nm long-pass filter. (f, h) Persistent luminescence of $ZnGa_2O_4:Cr^{3+}$ NPs, recorded within 2 seconds after stopping LED illumination and using a 600 nm long-pass filter.

Noteworthy, this is the first study to explore the uptake of top-down-prepared plastic nano- and microparticles labeled with PersL NPs in a biological model. To date, research on the uptake of micro- and nanoplastics has been mostly restricted to the particles prepared via bottom-up processes, such as atom-transfer radical polymerization.[54,55] As pointed out by Pradel et al., bottom-up prepared plastic models are less environmentally relevant than top-down prepared samples because their properties and aggregation behavior do not resemble the incidentally produced plastics.[1] Besides their monodisperse sizes, spherical shape, and smooth surface, bottom-up prepared micro- and nanoplastics are often grafted with surfactants or stabilizers used for their synthesis. However, even trace amounts of such compounds can affect the aggregation and interaction of plastics with biological membranes, subsequently influencing their uptake by organisms. In addition, the top-down approach limits the number of organic solvents used, and the solvent evaporation step assures its elimination prior to the biological tests.[56]

Since exposure to micro- and nanoplastics has become a major environmental problem and a growing public health concern worldwide, monitoring the uptake and dissemination of

environmentally relevant plastic models is a fundamental research task. Therefore, this work contributes to the area of microplastic research by demonstrating the uptake of polystyrene microparticles at a low-level trophic chain organism, *D. magna*.

4. Summary

Three synthesis methods were evaluated to obtain optimal inorganic persistent luminescence nanoparticles for labeling polystyrene for bioimaging applications: precipitation, hydrothermal, and solvothermal. Using these three approaches, we successfully synthesized and optimized $ZnGa_2O_4:Cr^{3+}$-based NPs. Despite employing identical ion ratios across all methods, the solvothermal route yielded the best results regarding persistent luminescence and nanoparticle morphology. The $ZnGa_2O_4:Cr^{3+}$ NPs synthesized via the solvothermal method were single-phase and exhibited small average sizes of approximately 2.8 ± 0.6 nm.

The composition of the NPs was further optimized to enhance luminescent performance. The most intense luminescence under UV excitation was observed for samples prepared with a Zn^{2+} to Ga^{3+} ratio of 1:2 and a Cr^{3+} doping concentration of 0.3%. The longest decay times of persistent luminescence—up to 9.8 seconds—were achieved with a Zn^{2+} to Ga^{3+} ratio of 1:1.8 and a Cr^{3+} concentration of 0.28%. Notably, all samples synthesized via the solvothermal method exhibited persistent luminescence lasting between 6.6 and 9.8 seconds, underscoring the critical role of the synthesis method. In contrast, nanoparticles produced via precipitation and hydrothermal methods displayed significantly shorter emission decays, not exceeding 2.2 seconds.

The optimized $ZnGa_2O_4:Cr^{3+}$ NPs were subsequently used to label polystyrene and fabricate luminescent plastic particles via cryomilling—a top-down approach. This process yielded irregularly shaped micro- and nanoplastics, which were then employed in biological experiments. The doped plastic particles retained the bright, long-lasting, persistent luminescence of $ZnGa_2O_4:Cr^{3+}$ NPs. This novel method enabled the tracking of microplastics through persistent luminescence emission within the first biological window. Consequently, persistent luminescence was successfully used to monitor microplastic uptake in aquatic organisms (*Daphnia magna*) for the first time.

Acknowledgments

The National Science Centre, Poland, funded this research under grant no. 2021/43/B/ST5/00046 and 2022/45/B/ST5/00604.

5. References

[1] A. Pradel, C. Catrouillet, J. Gigault, *NanoImpact* **2023**, *29*, 100453.

[2] R. C. Thompson, W. Courtene-Jones, J. Boucher, S. Pahl, K. Raubenheimer, A. A. Koelmans, *Science* **2024**, *386*, eadl2746.

[3] J. Lei, Q. Ma, X. Ding, Y. Pang, Q. Liu, J. Wu, H. Zhang, T. Zhang, *Environ Chem Lett* **2024**, *22*, 2913.

[4] B. Zhao, P. Rehati, Z. Yang, Z. Cai, C. Guo, Y. Li, *Science of The Total Environment* **2024**, *912*, 168946.

[5] J. Musial, D. T. Mlynarczyk, B. J. Stanisz, *Science of The Total Environment* **2023**, *856*, 159122.

[6] S. Zhuang, J. Wang, *Science of The Total Environment* **2023**, *897*, 165414.

[7] G. Bordós, B. Urbányi, A. Micsinai, B. Kriszt, Z. Palotai, I. Szabó, Z. Hantosi, S. Szoboszlay, *Chemosphere* **2019**, *216*, 110.

[8] A. Rossatto, M. Z. F. Arlindo, M. S. de Morais, T. D. de Souza, C. S. Ogrodowski, *Environmental Advances* **2023**, *13*, 100396.

[9] T. Bosker, G. Olthof, M. G. Vijver, J. Baas, S. H. Barmentlo, *Environmental Pollution* **2019**, *250*, 669.

[10] L. Zimmermann, S. Göttlich, J. Oehlmann, M. Wagner, C. Völker, *Environmental Pollution* **2020**, *267*, DOI: 10.1016/j.envpol.2020.115392.

[11] N. Yakovenko, B. Amouroux, M. Albignac, F. Collin, C. Roux, A. F. Mingotaud, P. Roblin, C. Coudret, A. ter Halle, *Environ Sci Nano* **2022**, *9*, 2453.

[12] S. Roch, A. Brinker, *Environ Sci Technol* **2017**, *51*, 4522.

[13] C. Di Fiore, Y. Ishikawa, S. L. Wright, *J Hazard Mater* **2024**, *464*, 132991.

[14] G. W. Xing, J. Gao, H. Wang, Y. C. Liu, *Molecules* **2023**, *28*, DOI: 10.3390/molecules28207102.

[15] Z. Gao, K. Wontor, J. V Cizdziel, *Molecules* **2022**, *27*, 7415.

[16] A. Mercedi, G. Gentili, V. Poli, C. Philipp, B. Rosso, M. C. Lavagnolo, I. Hallanger, F. Corami, M. Meneghetti, L. Litti, *ACS Omega* **2024**, DOI: 10.1021/acsomega.4c05693.

[17] J. Ornik, S. Sommer, S. Gies, M. Weber, C. Lott, J. C. Balzer, M. Koch, *Applied Physics B* **2020**, *126*, 15.

[18] M. v. DaCosta, S. Doughan, Y. Han, U. J. Krull, *Anal Chim Acta* **2014**, *832*, 1.

[19] T. Grzyb, S. Ryszczyńska, N. Jurga, D. Przybylska, I. R. Martín, *ACS Appl Mater Interfaces* **2024**, DOI: 10.1021/acsami.4c10176.

[20] N. Zhu, X. Wei, J. Yu, S. Zhang, D. Hu, P. Li, Y. Xia, K. Song, *Plants* **2023**, *12*, 2554.

[21] X. H. Lin, L. Song, S. Chen, X. F. Chen, J. J. Wei, J. Li, G. Huang, H. H. Yang, *ACS Appl Mater Interfaces* **2017**, *9*, 41181.

[22] Z. Zhou, W. Zheng, J. Kong, Y. Liu, P. Huang, S. Zhou, Z. Chen, J. Shi, X. Chen, *Nanoscale* **2017**, *9*, 6846.

[23] R. Zou, J. Huang, J. Shi, L. Huang, X. Zhang, K. L. Wong, H. Zhang, D. Jin, J. Wang, Q. Su, *Nano Res* **2017**, *10*, 2070.

[24] L. Song, P. P. Li, W. Yang, X. H. Lin, H. Liang, X. F. Chen, G. Liu, J. Li, H. H. Yang, *Adv Funct Mater* **2018**, *28*, 1.

[25] Y. Lin, J. Hu, L. Wu, Q. Zou, D. Chen, D. Huang, H. Lu, S. Bin Wang, H. Zhu, *J Mater Chem B* **2021**, *9*, 1131.

[26] M. N. Da Silva, J. M. De Carvalho, M. C. De Abreu Fantini, L. A. Chiavacci, C. Bourgaux, *ACS Appl Nano Mater* **2019**, *2*, 6918.

[27] C. Lee, D. Park, W.-T. Shiu, Y. Liu, L. Liu, *Nanomaterials* **2025**, *15*, 247.

[28] A. Drozdowski, D. Poelman, M. Runowski, H. Hemmerich, F. Rivera-López, T. Grzyb, *J Mater Chem C Mater* **2024**, *12*, 13040.

[29] J. Gao, L. Yuan, Y. Min, M. Cao, H. Zhu, J. Hong, B. Yu, H. Cong, *Chemical Engineering Journal* **2025**, *505*, 159183.

[30] D. Li, Y. Wang, K. Xu, H. Zhao, Z. Hu, *Opt Mater (Amst)* **2014**, *36*, 1836.

[31] M. K. Hussen, F. B. Dejene, *Optik (Stuttg)* **2019**, *181*, 514.

[32] S. Rafiezadeh, C. Irvine, A. K. Salih, M. Mousavi, M. R. Phillips, M. B. Ghasemian, C. Ton-That, *ACS Appl Nano Mater* **2025**, *8*, 1033.

[33] B. Qi, W. Dai, B. Lou, B. Song, Z. Miao, Y. Wei, C. Ma, J. Wang, *ACS Nano* **2025**, *19*, 5818.

[34] R. Zou, S. Gong, J. Shi, J. Jiao, K. L. Wong, H. Zhang, J. Wang, Q. Su, *Chemistry of Materials* **2017**, *29*, 3938.

[35] Y. Katayama, H. Kobayashi, S. Tanabe, *Applied Physics Express* **2015**, *8*, 2.

[36] L. Huang, L. Lin, W. Xie, Z. Qiu, H. Ni, H. Liang, Q. Tang, L. Cao, J. X. Meng, F. Li, *Chemistry of Materials* **2020**, *32*, 5579.

[37] X. Song, W. Zhuang, H. Cui, M. Liu, T. Gao, A. Li, Z. Gao, *Science of The Total Environment* **2022**, *838*, 156068.

[38] X. Zhao, J. Sun, L. Zhou, M. Teng, L. Zhao, Y. Li, F. Wu, *Environ Sci Nano* **2023**, *10*, 2634.

[39] N. P. Ivleva, *Chem Rev* **2021**, *121*, 11886.

[40] F. Abdolahpur Monikh, M. G. Vijver, D. M. Mitrano, H. A. Leslie, Z. Guo, P. Zhang, I. Lynch, E. Valsami-Jones, W. J. G. M. Peijnenburg, *Nano Today* **2021**, *41*, 101296.

[41] M. Wang, W.-X. Wang, *J Hazard Mater* **2023**, *458*, 131864.

[42] A. Krzynowek, B. Van de Moortel, N. Pichler, I. Vanoverberghe, J. Lapere, L. M. Jenisch, D. Deloof, W. Thielemans, K. Muylaert, M. Dusselier, D. Springael, K. Faust, E. Decaestecker, *ISME J* **2024**, DOI: 10.1093/ismejo/wrae234.

[43] J. Yin, Y. Long, W. Xiao, D. Liu, Q. Tian, Y. Li, C. Liu, L. Chen, Y. Pan, *Ecotoxicol Environ Saf* **2023**, *249*, 114433.

[44] A. Fernández-Osorio, M. Tapia, A. R. Vázquez-Olmos, J. Chávez, *J Solid State Chem* **2019**, *269*, 328.

[45] L. Li, Y. Wang, H. Huang, H. Li, H. Zhao, *Modern Physics Letters B* **2016**, *30*, 9.

[46] Z. Gyri, V. Havasi, D. Madarász, D. Tátrai, T. Brigancz, G. Szabó, Z. Kónya, Á. Kukovecz, *J Mol Struct* **2013**, *1044*, 87.

[47] L. Sørensen, M. H. Gerace, A. M. Booth, *Cambridge Prisms: Plastics* **2024**, *2*, e13.

[48] N. B. Hartmann, T. Hüffer, R. C. Thompson, M. Hassellöv, A. Verschoor, A. E. Daugaard, S. Rist, T. Karlsson, N. Brennholt, M. Cole, M. P. Herrling, M. C. Hess, N. P. Ivleva, A. L. Lusher, M. Wagner, *Environ Sci Technol* **2019**, *53*, 1039.

[49] L. Eitzen, S. Paul, U. Braun, K. Altmann, M. Jekel, A. S. Ruhl, *Environ Res* **2019**, *168*, 490.

[50] A. F. Astner, D. G. Hayes, H. O'Neill, B. R. Evans, S. V. Pingali, V. S. Urban, T. M. Young, *Science of The Total Environment* **2019**, *685*, 1097.

[51] J. Caldwell, R. Lehner, S. Balog, C. Rhême, X. Gao, D. Septiadi, C. Weder, A. Petri-Fink, B. Rothen-Rutishauser, *Environ Sci Nano* **2021**, *8*, 502.

[52] D. Przybylska, N. Jurga, A. Ekner-Grzyb, N. Stopikowska, B. F. Grześkowiak, M. Runowski, T. Grzyb, *Adv Opt Mater* **2024**, *12*, DOI: 10.1002/adom.202401499.

[53] S. Ryszczyńska, K. Soler-Carracedo, A. Ekner-Grzyb, N. Jurga, M. Ćwierzona, D. Piątkowski, T. Grzyb, *Adv Opt Mater* **2025**, *13*, DOI: 10.1002/adom.202402053.

[54] S. Ducoli, G. Kalčíková, M. Velimirovic, L. E. Depero, S. Federici, *Environ Chem Lett* **2025**, *23*, 649.

[55] F. Hao, Z. Y. Yan, Z. Wang, X. P. Yan, *Anal Chem* **2024**, *96*, 10662.

[56] Y. Liu, J. Li, B. V. Parakhonskiy, R. Hoogenboom, A. Skirtach, S. De Neve, *J Hazard Mater* **2024**, *462*, 132785.